Simulation of Late Cenozoic South American Flat-Slab Subduction Using Geodynamic Models with Data Assimilation

Article *in* Earth and Planetary Science Letters · March 2016

DOI: 10.1016/j.epsl.2016.01.011

CITATIONS
11

READS
668

4 authors, including:

Jiashun Hu
University of Illinois, Urbana-Champaign
7 PUBLICATIONS **18** CITATIONS
SEE PROFILE

Lijun Liu
University of Illinois, Urbana-Champaign
73 PUBLICATIONS **986** CITATIONS
SEE PROFILE

Quan Zhou
University of Illinois, Urbana-Champaign
8 PUBLICATIONS **20** CITATIONS
SEE PROFILE

Earth and Planetary Science Letters 438 (2016) 1–13

Contents lists available at ScienceDirect

Earth and Planetary Science Letters

www.elsevier.com/locate/epsl

Simulation of late Cenozoic South American flat-slab subduction using geodynamic models with data assimilation

Jiashun Hu *, Lijun Liu, Armando Hermosillo, Quan Zhou

Department of Geology, University of Illinois at Urbana-Champaign, 605 E. Springfield Ave, Champaign, IL, 61820, USA

ARTICLE INFO

Article history:
Received 29 August 2015
Received in revised form 25 November 2015
Accepted 9 January 2016
Available online xxxx
Editor: B. Buffett

Keywords:
South America
flat slab
aseismic ridge
oceanic plateau
suction force
seafloor age

ABSTRACT

The formation mechanisms of flat slabs in South America remain unclear. To quantitatively evaluate the earlier proposed mechanisms, we simulate the post-100 Ma subduction history below South America using 4-D geodynamic models by progressively incorporating plate kinematics, seafloor ages and key tectonic features including the buoyant oceanic crust, continental cratons, oceanic plateaus (i.e. the inferred Inca plateau, subducting Nazca Ridge and Juan Fernandez Ridge), as well as deformable trench profiles according to recent geological reconstructions. We find that, in the absence of an overriding plate and subducting buoyancy features, the seafloor age affects slab dip angle by controlling the slab's mechanical strength (i.e., the resistance to bending) and negative buoyancy (integrated positive density anomaly that enhances bending). Our models show that slab strength dominates its buoyancy at age >30 Ma and the opposite for younger ages. The existence of a thick overriding plate reduces the slab dip by increasing dynamic suction, and individual cratonic roots further lead to along-trench variations of dip angle reduction. While dynamic suction from the overriding plate generates a permanent reduction of the long-wavelength slab dip angle, it is the final addition of subducting oceanic plateau and aseismic ridges that produces the transient and localized flat-slabs as observed. These results suggest that all mechanisms except the buoyancy features affect the slab dip only at large spatial scales. Our best-fit model with all the above tectonic features included provides a good match to both the upper mantle Benioff zones and the temporal evolution of volcanic arcs since the mid-Miocene. The imperfect match of the Peruvian flat-slab is likely associated with the uncertain 3-D configuration of the Amazonian craton.

Published by Elsevier B.V.

1. Introduction

South America has the longest continuous subduction zone in the world that stretches 7500 km from ~10°N to ~60°S (Klotz et al., 2001). Subduction along this ocean–continent convergent boundary started no later than the Cretaceous during the final separation of supercontinent Pangaea (Müller et al., 2008). South America, therefore, provides an ideal test yard for understanding subduction dynamics and the associated mantle processes. The present South American subduction zone is characterized by along-strike variation of slab dipping angles. There are several segments of flat slab including Bucaramanga, Peruvian and central Chile flat slabs (Gutscher et al., 2000), which are intervened by normal to steep subduction (Fig. 1).

In theory, the dip angle of a subducting slab is controlled by two competing forces, the negative buoyancy (i.e., integrated density anomaly) of the slab and resistance from the surrounding mantle and the overriding lithosphere (Stevenson and Turner, 1977). Over the past several decades, a number of possible mechanisms have been proposed to explain the formation of flat-slab subduction. These mechanisms include: (a) the subduction of buoyancy anomalies such as oceanic plateaus, aseismic ridges, and seamount chains (Cloos, 1993; Gutscher et al., 1999a; van Hunen et al., 2002; Mason et al., 2010); (b) the fast active overriding of a continent over young oceanic lithosphere (van Hunen et al., 2000); (c) the hydrodynamic suction force due to thick continental roots that couples the subducting slab with the overriding plate (Jones et al., 2011; Roda et al., 2011; Rodríguez-González et al., 2012; O'Driscoll et al., 2009, 2012).

According to recent plate reconstructions (Müller et al., 2008; Seton et al., 2012), South America has not experienced exceptionally fast westward motion since the Cretaceous, implying that the fast overriding continent mechanism may not apply to South America, but the young oceanic lithosphere may play a role. Among existing studies, Gutscher et al. (2000) and Anderson et al. (2007) proposed that the central Chile flat slab, one of the most prominent flat slabs in South America, may be flattened by the

* Corresponding author.
E-mail address: jhu16@illinois.edu (J. Hu).

http://dx.doi.org/10.1016/j.epsl.2016.01.011
0012-821X/Published by Elsevier B.V.

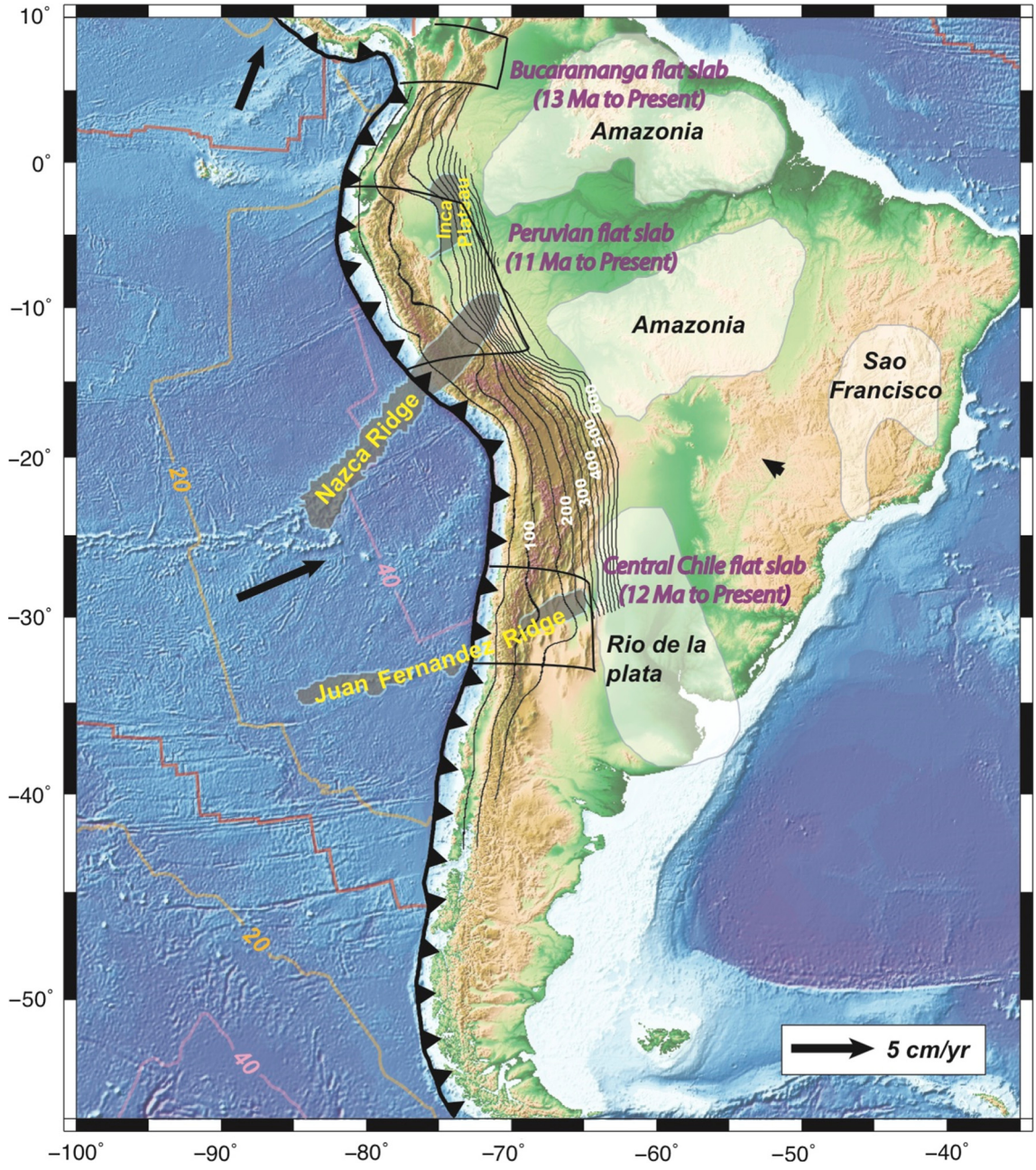

Fig. 1. Geological setting of South America with depth contours of slab 1.0 (Hayes et al., 2012) indicated by thin black lines, subducting oceanic plateaus translucent gray and continental cratons translucent white. The major flat slabs in South America are outlined with thick black lines. The locations of oceanic plateaus, cratons and flat slabs are modified from Gutscher et al. (2000), Loewy et al. (2004) and Ramos and Folguera (2009), respectively. The present-day plate motion is shown as black arrows. Tooth-shaped line represents the South American trench. Seafloor ages to the west of South America are shown with colorful lines with numbers indicating the age in Ma.

Juan Fernandez Ridge. However, the same flat slab was also attributed to the suction force of the Rio de la plata craton (Manea et al., 2012). For the Peruvian flat slab, Gutscher et al. (1999a) argued that it was due to subduction of the "lost Inca plateau" and the Nazca Ridge, although in theory it could also be influenced by the thick Amazonian craton (O'Driscoll et al., 2009, 2012).

In contrast, some studies proposed that moderate-sized buoyancy features could not result in significant slab flattening (Martinod et al., 2005; Gerya et al., 2009). Furthermore, if the basalt-to-eclogite transformation finishes at shallow depths (<70 km), the subduction of oceanic plateau would prohibit the formation of flat slabs (Arrial and Billen, 2013). It is also suggested that the correlation between South American flat slabs and subducting bathymetric highs is rather poor (Skinner and Clayton, 2013). These existing debates raise the need for a systematic evaluation of the different mechanisms for the formation of flat-slab subduction in South America.

Here we report the first 4D quantitative geodynamic modeling on the subduction history of South America. We test both the respective and accumulative effects of seafloor age variation, hydrodynamic suction, and buoyancy feature subduction on the formation of flat slabs. These mechanisms influence the slab dip angle by controlling the negative buoyancy and mechanical strength (i.e., resistance to bending) of the slab, reducing the dynamic pressure in the mantle wedge, and decreasing slab density locally, respectively. By incorporating all these physical processes in the subduction models, we attempt to predict the present-day slab geometry and the temporal evolution of flat-slab formation, which

are evaluated with the distribution of deep seismicity (Hayes et al., 2012) and volcanic arc migration from the online catalog of Peruvian Mining and Metallurgical Geological Institute – INGEMMET (http://www.ingemmet.gob.pe).

Among the three present-day flat-slab segments in South America (Barazangi and Isacks, 1976, 1979; Pennington, 1981; Ramos et al., 2002; Ramos and Folguera, 2009), the central Chile flat-slab (i.e. Pampean flat slab) that has been in existence since ~12 Ma currently extends from 27° to 33°30′S, the Peruvian flat-slab existing since 11 Ma extends from 5° to 14°S, and the Bucaramanga flat-slab since ~13 Ma covers 5° to 9°N. Here, we mainly focus on the present-day Central Chile and Peruvian flat slabs, since the Bucaramanga segment is too close to the edge of our model domain.

2. Model setup

We use the 3D spherical finite element code CitcomS (Zhong et al., 2000; Tan et al., 2006) to simulate subduction and mantle convection. Our model domain extends from 10°W to 100°W in longitude, from 70°S to 20°N in latitude, and covers the whole mantle in depth. It is discretized with $257 \times 257 \times 65$ nodes in latitude × longitude × depth using a spatially variable finite-element mesh, with the finest resolution of $27 \times 27 \times 8$ (km) occurring in the central 2/3 of the mesh.

2.1. Governing equations

We solve the thermal–chemical mantle convection following the conservation of mass, momentum and energy. We assume the mantle flow is incompressible, with a variable viscosity structure, and satisfies the Boussinesq approximation. The governing equations are:

$$\nabla \cdot \vec{u} = 0 \tag{1}$$

$$-\nabla P + \nabla \cdot \left[\eta\left(\nabla\vec{u} + \nabla^T\vec{u}\right)\right] + (\rho_m \alpha \Delta T + \Delta\rho_c)\vec{g} = 0 \tag{2}$$

$$\frac{\partial T}{\partial t} + \vec{u} \cdot \nabla T = \kappa \nabla^2 T \tag{3}$$

$$\frac{\partial C}{\partial t} + \vec{u} \cdot \nabla C = 0 \tag{4}$$

where $\vec{u}$ is velocity, P is dynamic pressure, T temperature, ρ_m ambient mantle density, $\Delta\rho_c$ compositional density anomaly, ΔT temperature anomaly, η dynamic viscosity, α thermal expansion coefficient, κ thermal diffusivity, $\vec{g}$ gravitational acceleration, and C composition, respectively.

In Equation (2), both thermal and compositional buoyancy are taken into account. Equation (4) describes the advection of chemical particles, and this is solved using a ratio method for Lagrangian particles (Tackley and King, 2003).

2.2. Boundary conditions

The model utilizes the plate kinematics and seafloor age evolution from the plate reconstruction of Müller et al. (2008) to update the surface velocity boundary condition and the upper thermal boundary layer profile, respectively (Figs. 2a–c). All other boundaries are free slip. The core–mantle boundary has a fixed temperature that is set to be the background mantle temperature. The surface velocity and seafloor age are reconstructed over an interval of 1 Ma, using the open source paleo-geographic software GPlates (www.gplates.org/; Gurnis et al., 2012). At any given time within the interval, we linearly interpolate the surface velocity and seafloor age. We also take into account the history of central Andean deformation (Fig. 2d) by changing the trench profile through time using the most recent Andean shortening reconstruction (Arriagada et al., 2008).

The model assimilates the seafloor age at each time step to update the top thermal boundary layer within oceanic plates, where we define an error function distribution of thermal profile. In order to overcome the numerical diffusion which exists within the top thermal boundary layer as the finite grid resolution would smear out the sharp thermal gradient in the boundary layer (Davies et al., 2007; Liu and Stegman, 2011), we reduce the thermal gradient across the boundary layer from ~1200 °C to ~700 °C while maintaining the total buoyancy of the boundary layer unchanged by applying an age-dependent correction to the error function (similar to Liu and Stegman, 2011). The continent is assumed at the ambient mantle temperature, in order to maintain its overall neutral buoyancy.

2.3. Rheology

Three-dimensional temperature- and composition-dependent viscosity is applied in the model. The background mantle viscosity follows a 4-layer profile (Fig. 2e): lithosphere (0–100 km), asthenosphere (100–300 km), transition zone (300–660 km), and lower mantle (660–2890 km). Their respective viscosity values are 10^{23}, 3×10^{19}, 10^{21}, and 3×10^{22} Pa s. In the lower mantle, the viscosity increases from 3×10^{22} Pa s right below 660 km depth to 10^{23} Pa s at >1200 km, and then gradually decreases below 2000 km toward the core–mantle boundary to 3×10^{22} Pa s. Such a viscosity profile is obtained by matching the present-day mantle seismic structure with predicted slab geometry. This profile is also consistent with recent petrological experiment by Marquardt and Miyagi (2015), suggesting a significantly increased strength of ferropericlase in the upper part of lower mantle. This is further supported by the observation of global slab stagnancy above 1000 km depth from recent tomography images (Fukao and Obayashi, 2013).

In order to facilitate subduction, the model has also incorporated sharp lateral viscosity variations, including a weak zone (with a viscosity of 10^{19} Pa s) along the subduction zone and a weak mantle wedge above the down-going slab, similar to earlier models by Liu and Stegman (2011). To simulate the dynamic suction force from cratons, we prescribe these continental units as high-viscosity bodies. We first define a 75–100-km thick continental lithosphere, and then prescribe individual cratonic roots, which extends to about 200 km depth. The geometry of cratonic roots at 75 km depth is defined according to Loewy et al. (2004) (Fig. 1). The area of the roots shrinks as it goes from the surface to 200 km depth, in order to avoid a step-like craton viscosity profile. These high-viscosity features regulate the flow pattern in the upper mantle and generate suction force to flatten the slab.

2.4. Implementation of oceanic crust, plateau and mid-ocean ridges

We use compositional tracers to define the oceanic crust and the oceanic plateaus. The geometry of Inca Plateau, Nazca Ridge and Juan Fernandez Ridge are prescribed according to Gutscher et al. (2000) (Fig. 1). These features are embedded in the subducting oceanic plate. We assume that the oceanic crust is 8 km thick with a density of 2.9 g/cm^3, and that the oceanic plateau and aseismic ridges are 15 km thick with the same density. These features reduce the density of the down-going slab, and thus could potentially flatten the slab. We simulate the density change due to basalt-to-eclogite phase transformation by turning off tracer buoyancy at ~100 km depth for both the crust and oceanic plateaus.

The oceanic crust is implemented into the model since 100 Ma. As seafloor spreads, new oceanic crust forms at the mid-ocean ridge where the seafloor is young. We update the composition of young seafloors (<10 Ma) at each time step, in order to mimic the oceanic crust generation along mid-ocean ridges. We introduce the Inca Plateau, Nazca Ridge and Juan Fernandez Ridge into

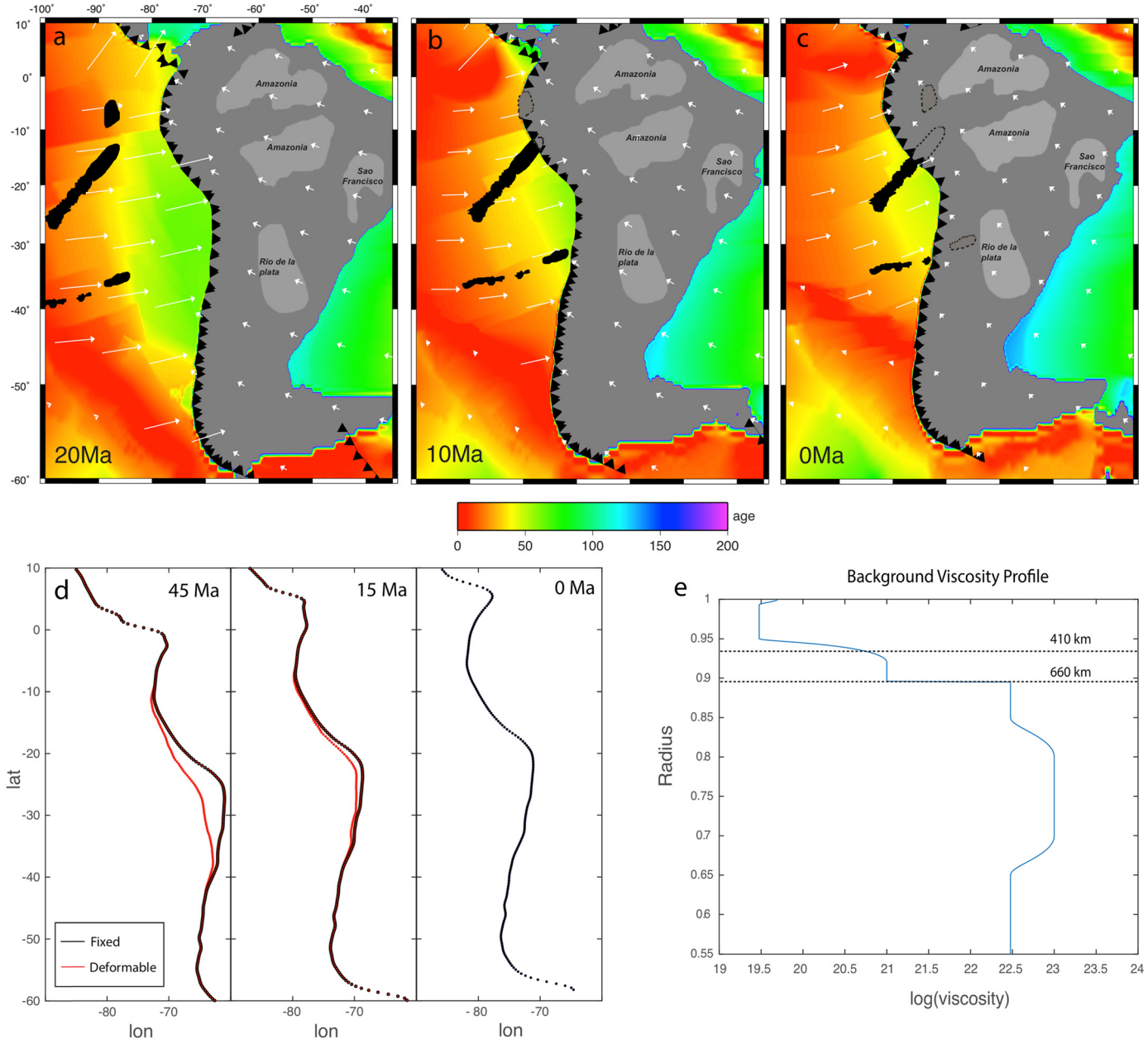

Fig. 2. Surface velocity boundary conditions and seafloor age distribution at (a) 20 Ma, (b) 10 Ma and (c) present. White arrows show the direction and magnitude of surface velocities. Background color represents the seafloor age. Black regions represent the oceanic plateau and aseismic ridges with dashed contours indicating the already-subducted parts. The South American continent is shown with dark gray with cratons indicated by light gray. (d) Trench profiles at 45 Ma, 15 Ma and present. Red lines indicate the temporally deformable trench profiles (Arriagada et al., 2008), and black lines represent the present-day trench geometry. (e) Background 1D mantle viscosity structure. Key features include a low-viscosity asthenosphere and a viscosity maximum in the upper part of the lower mantle. (For interpretation of the references to color in this figure legend, the reader is referred to the web version of this article.)

the model at 15 Ma, with their initial configuration reconstructed starting from their present-day positions (Gutscher et al., 2000) using past plate motions (Müller et al., 2008) with GPlates (Boyden et al., 2011). In our model, the subduction of Inca Plateau and Nazca Ridge began at ~12 Ma and that of Juan Fernandez Ridge began at ~9 Ma. We realize the uncertainty in the earlier subducted length of Juan Fernandez Ridge (Yáñez et al., 2002; Kay and Mpodozis, 2002), but the simulation of a longer ridge subduction history results in a similar present-day slab structure to that of a shorter history. This may be related to the change of the ridge's strike orientation in the past and its southward migration relative to South America (Huene et al., 1997). We conclude that only the recent subduction history (post-10 Ma) of the ridge has contributed to the formation of the Central Chile flat slab.

2.5. Assimilation of a deformable South American trench

There are multiple palinspastic reconstructions of the Cenozoic shortening of the central Andes (Isacks, 1988; Kley and Monaldi, 1998; McQuarrie, 2002; Oncken et al., 2006; Arriagada et al., 2008). Among these reconstructions, we choose the one from Arriagada et al. (2008) to represent the trench profile evolution during the geological past. This is because their model incorporates the most extensive tectonic shortening events and paleomagnetically determined tectonic rotations.

In practice, we first collect the trench profiles at 45, 15, and 0 Ma from the reconstruction by Arriagada et al. (2008) (there was no significant shortening before 45 Ma). We then linearly interpolate these trench profiles and calculate the shortening rate at any

given time and space, assuming shortening occurs only along the east–west direction. To the first order, this is a valid approximation, since the convergence rate between the Farallon/Nazca plate and South American plate was mainly along the east–west direction during the past 100 Ma (e.g., Müller et al., 2008). After we obtain these trench profiles, we rotate them back in time, in order to get the absolute locations of the South American trench history (Fig. 2d).

Subsequently, we update both the velocity and thermal boundary conditions according to these deformable trench locations. The shortening of the overriding plate was accommodated in a zone of ~700 km width behind the trench, where the shortening rate decreases linearly inland-ward. Effectively, our approach may be similar to the one by Gurnis et al. (2013) and Flament et al. (2014), and their approach also requires substantial work in code-development and data-compilation.

3. Results

In this section, we present model results testing various physical mechanisms for flat-slab formation, and the predicted modern slab configuration in South America.

3.1. The physical mechanisms for flat-slab formation

As discussed in section 1, among earlier proposed mechanisms for flat-slab formation, those relevant to South American subduction include dynamic suction caused by strong cratonic roots inside the overriding plate (Manea et al., 2012), subduction of intra-slab buoyancy anomalies associated with aseismic ridges and oceanic plateaus (Gutscher et al., 1999a), and subduction of young seafloors (van Hunen et al., 2000). In this paper, we attempt to evaluate the relative contributions of these different mechanisms for the resulting present-day slab geometry.

3.1.1. Seafloor age

To explore the seafloor age effect, we first design two different models: one has a uniform seafloor age of 30 Myr during the entire subduction history (model I), and the other has temporal-spatial variations of seafloor age (model II) derived from the plate reconstruction of Müller et al. (2008) (Fig. 2). These two models do not include a high-viscosity overriding plate and intra-slab buoyancy features in order to isolate the effect of seafloor age. In model I, the present-day slab subducts steeply along the entire trench (Figs. 3a, 4). In contrast, the slab in model II is shallower almost everywhere along the trench (Figs. 3b, 4). The slab dip angle (defined by the upper surface of the slab between the trench and at 200 km-depth, Fig. 5b) varies along the trench, with two shallow-dipping slab segments centered at ~10°S and ~29°S, respectively (Figs. 3a, 4). Since the only difference between models I and II is the seafloor age distribution (Fig. 3a, b), their different dip angles reflect the competition between the slab negative buoyancy and mechanical strength. However, the dependence of this competition, therefore slab dip, on seafloor age is elusive. For example, compared to model I, both younger (<30 Ma, north of 10°S and south of 30°S) and older (>30 Ma, between 10°S and 30°S) seafloors lead to shallower subduction in model II, although we do observe a larger dip angle reduction at the central part of the trench where seafloor is older.

In order to better discern the effect of seafloor age on slab dip, we run an additional model with a uniform seafloor age of 50 Ma (model S), an age similar to the oldest part (between ~15°S and ~30°S) of that in model II at the present day (Fig. 4). The predicted present-day slab in model S is systematically shallower than that in model I. It is also shallower than the slab in model II, except for the central portion (Fig. 4), where the two models have similar seafloor ages (Fig. 2a–c). Comparing model I (uniform age at 30 Ma) and model S (uniform age at 50 Ma), we can see that older seafloor age tends to induce shallower subduction, which suggests that slab mechanical strength dominates the effect of negative buoyancy on slab bending. This conclusion can also be drawn from the comparison of model II and model S, where between ~15°S and ~30°S, the slab dip angles in the two models are similar, consistent with their similar seafloor ages in this region; while in the other regions, the slab of model S is clearly shallower, corresponding to its older seafloor ages. Together with the comparison between models I and II, we suggest that for seafloor ages >30 Ma, the slab strength dominates its negative buoyancy in determining the slab dip, and that this relation reverses for ages <30 Ma. It is worth noting that, between ~25°S and ~30°S, all three models have close slab dip angles, which is largely related to the anchoring effect of slabs at greater depth due to early subduction, a topic outside the scope of this paper. Furthermore, in model I, the sharp kinks in slab dip distribution between ~15°S and ~20°S (Fig. 4) may be related to the variation of trench curvature (Fig. 3b).

Overall, with the tectonically reconstructed seafloor age history (i.e. model II), the predicted present-day slab dip angle distribution along trench is opposite to that outlined with Benioff zones, where shallow-to-flat slabs occur both north and south of central Andes (Figs. 1, 3b). Furthermore, the predicted subduction dip angle is consistently steeper than that observed (Fig. 3b). We note that, although an increase in the background mantle viscosity or slab strength could lead to shallower slabs, it would not explain the N–S variation of slab dip angle. This suggests that additional physical mechanisms are needed in order to explain the observed slab geometry.

3.1.2. Hydrodynamic suction

In order to investigate the effect of hydrodynamic suction, we perform two additional models, which have a uniform 100 km-thick overriding plate (model III) and a uniform 75 km-thick overriding plate with three 200 km-thick embedded cratons (model IV), respectively. Compared with model II, inclusion of a mechanically strong overriding plate (model III) leads to a reduction of slab dip along most of the South American trench (Figs. 3c, 5, 6). Addition of thick cratons (Amazonia, Sao Francisco, and Rio de la plata cratons; Fig. 1) inside the continent (model IV) reduces the dip angle further and generates long-wavelength (>1000 km) low-amplitude perturbations to the slab dip distribution (Figs. 3d, 5). This is due to enhanced hydrodynamic suction force from the overriding continent, which is reflected as a reduction of dynamic pressure inside the mantle wedge (Figs. 7, 8) (Stevenson and Turner, 1977; Manea et al., 2012). Among models II, III and IV, the magnitude of dynamic pressure reduction in the mantle wedge increases progressively (Fig. 7b–d), resulting in shallower and shallower slabs (Figs. 3b–d, 6). Physically, the reduction of dynamic pressure in the mantle wedge, and thus increased suction force, results from the existence of a high-viscosity overriding plate which confines the mantle flow to occur within a narrow region (Fig. 7; Stevenson and Turner, 1977). In a vertical profile, when a thick overriding plate exists, the lowered dynamic pressure occurs inside a very broad upper mantle region above the slab (Fig. 8), with the lowest pressure present in the asthenosphere whose viscosity is the lowest.

In addition to confirming earlier studies on the origin of hydrodynamic suction force (Manea and Gurnis, 2007; Manea et al., 2012), our results further quantify the magnitude and spatial pattern of this force associated with the 3D geometry of the overriding plate including cratonic roots. The observation that the predicted slab dips at the long-wavelength in models III and IV are close to that observed suggests that their predicted magnitude of suction force is reasonable, and a further increase of suction force

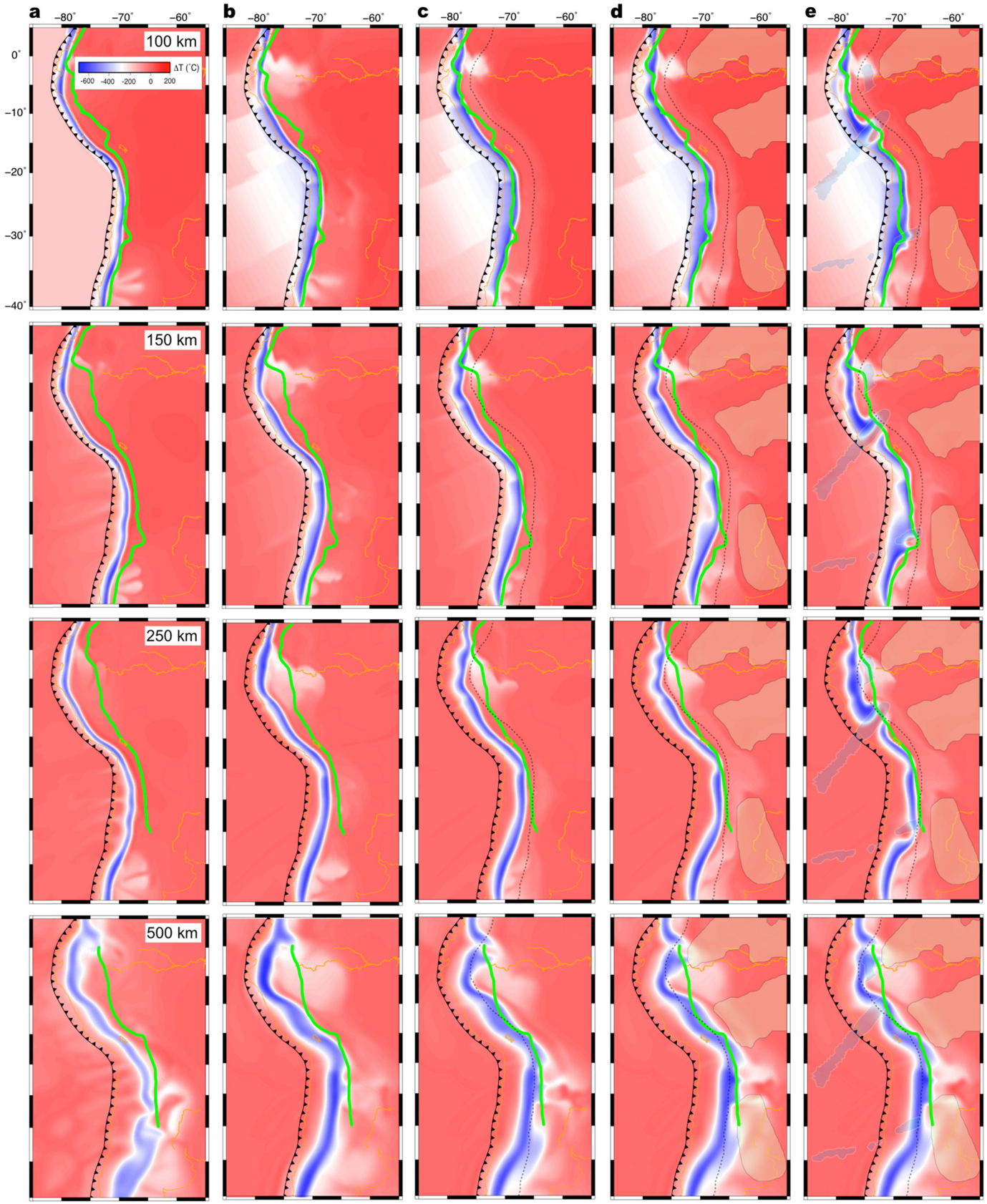

Fig. 3. Comparison of present-day slab geometry from five different subduction models. (a–e) Predicted slab geometry (blue color) from models I, II, III, IV and V (see main text), respectively. Different rows show different depths with the first row at 100 km, the second at 150 km, the third at 250 km, and the fourth at 500 km depth. Green lines represent the interpolated Benioff zones from *slab 1.0* (Hayes et al., 2012). Present-day configuration of the cratons and buoyancy features are shown with brown and blue, respectively, where we assume no lateral distortion in the geometry of the buoyancy features after subduction. Dotted lines outline the overriding plate. Note the progressive flattening of the slab from model I to model V. (For interpretation of the references to color in this figure legend, the reader is referred to the web version of this article.)

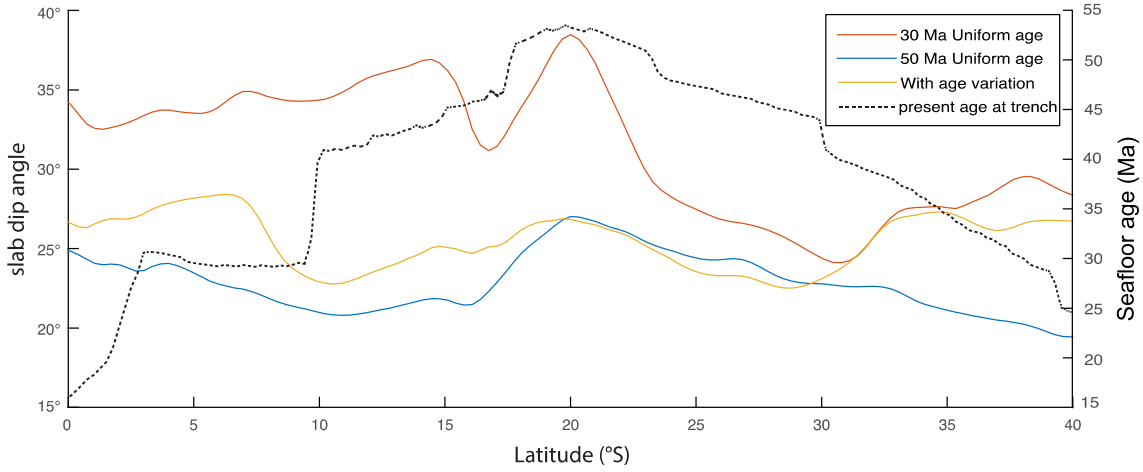

Fig. 4. Along-trench slab dip angle distribution (solid lines) from models I, II, and S and the present-day seafloor age distribution at trench (dashed line) in model II. Note the similar seafloor age distributions from 10 Ma to the present, the period relevant to the modern flat slab formation. Slab dip angle is measured according to the horizontal distance between the trench and the slab surface at 200 km depth along the east–west direction. Slab surface is defined as the upper interface between the slab and the ambient mantle, where the interface is the isotherm of 300 °C cooler than the ambient mantle.

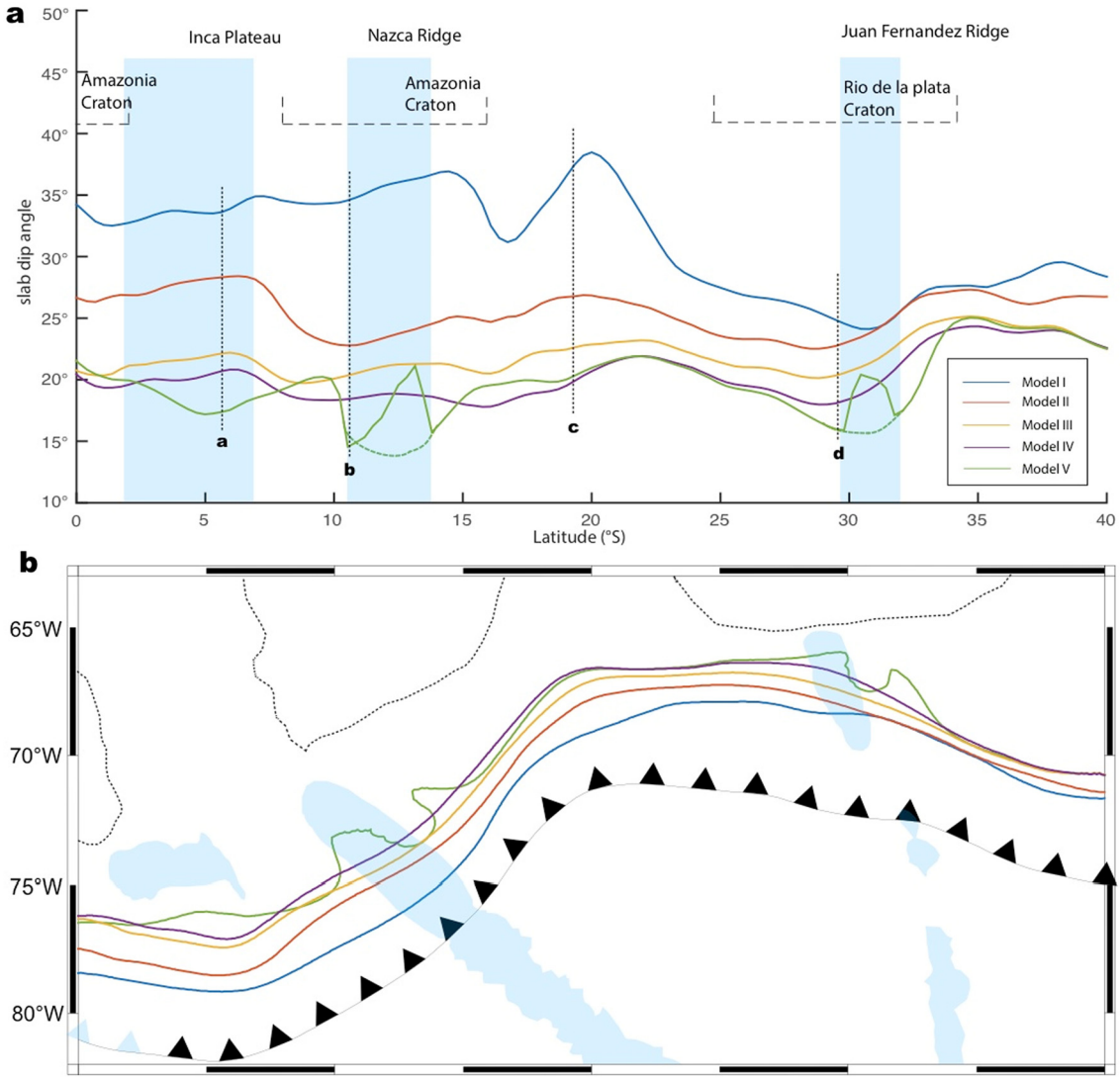

Fig. 5. (a) Present-day slab dip angle distribution along South American trench in models I, II, III, IV and V. The locations of subducting buoyancy features are marked with light blue, while the location of continental cratons are shown with dashed brackets. The dotted lines mark the location of the cross sections shown in Fig. 6. (b) Slab upper surface (300 °C cooler than the ambient mantle) at 200 km depth for the five models. Dashed lines outline the cratons, and light blue represents the buoyancy features. (For interpretation of the references to color in this figure legend, the reader is referred to the web version of this article.)

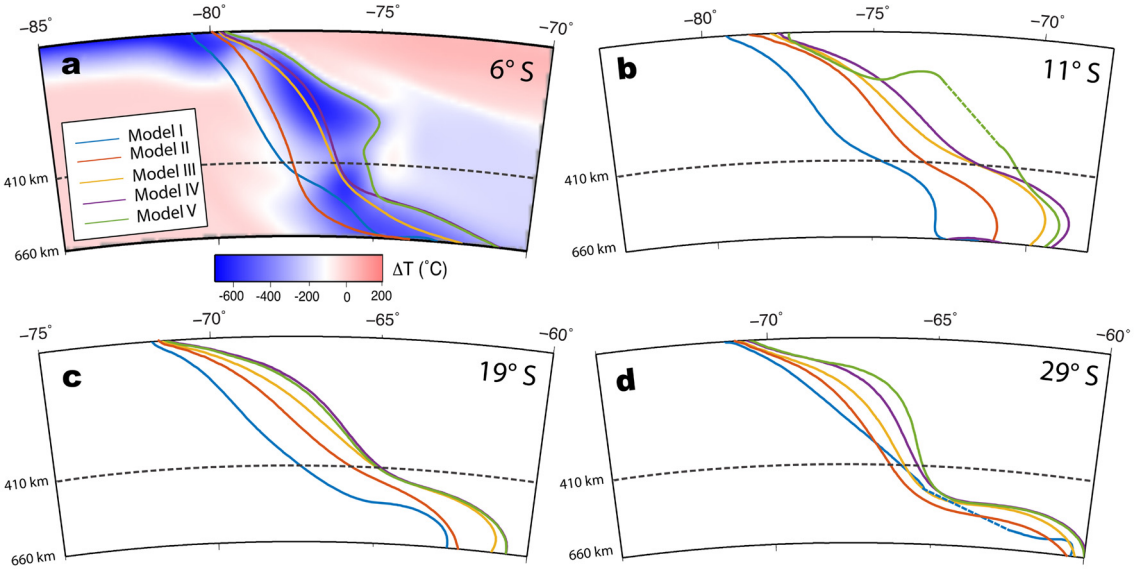

Fig. 6. Comparison of the slab upper surface of models I, II, III, IV and V at (a) 6°S, (b) 11°S, (c) 19°S and (d) 29°S, respectively, corresponding to the dashed lines in Fig. 5a. Notice the progressive flattening of the slabs across different models.

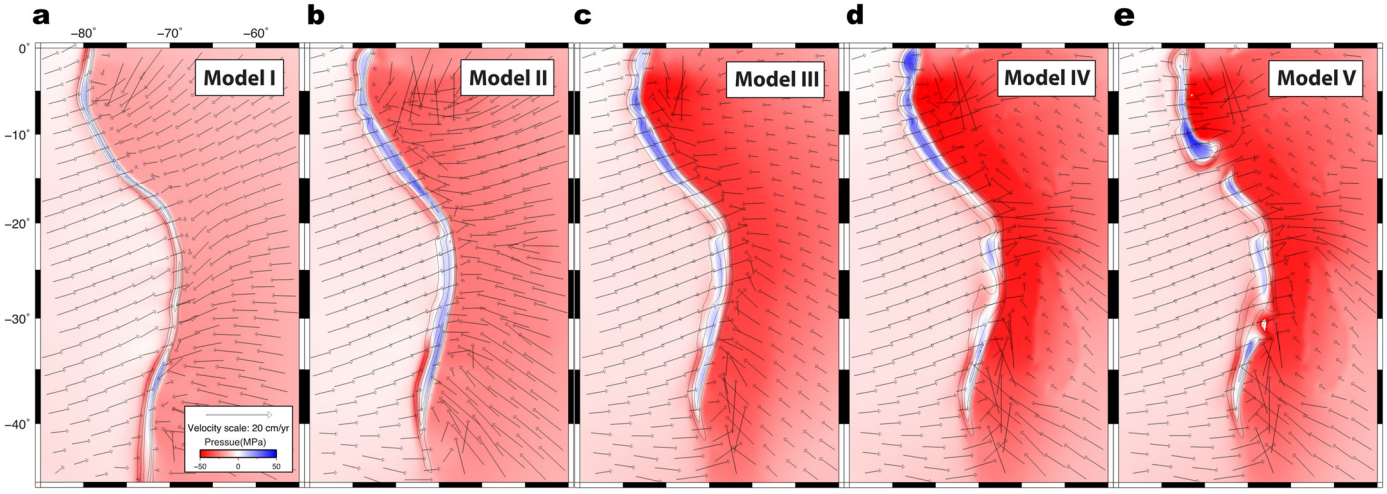

Fig. 7. Maps showing the dynamic pressure distribution at 140 km depth for models (a) I, (b) II, (c) III, (d) IV and (e) V. The mantle flow field is over-plotted as arrows. Thin black contours indicate slab isotherms with an increment of 100 °C. The dynamic pressure in mantle wedge is progressively lowered from model I to model IV.

would over-predict the flattening of slabs along most of the trench. Relative to model II, the reduction of slab dip angle in model IV is larger than that in model III, especially along the segments between ∼10° and 17°S and between ∼25° and 33°S, which correspond to the locations of the Amazonia and Rio de la plata cratons (Fig. 5a). This is because these cratons further confine the nearby mantle flow, resulting in greater suction (Fig. 7d).

In summary, model IV predicts the observed slab dip angles slightly better than model III, but both models still fail to predict the localized flat slabs in Southern Peru and Central Chile (Fig. 3c, d). In fact, the central South American trench flattening is already over predicted at depths above 150 km, but the northern and southern parts, especially the two flat-slab segments, are still under predicted. We do not attempt to improve this fit by tuning the thickness and viscosity profile of these cratons, because, first, geometry of these craton roots is not well constrained in observation; second, suction-induced flat slabs are likely permanent in time (Manea et al., 2012; Taramón et al., 2015), inconsistent with the recent history of these flat slabs. Finally, the fact that the width of the central Chile flat slab (Fig. 1) is much smaller than that of the Rio de la plata craton (thus the dimension of suction-induced permanent flat slab) dismisses a direct causal relationship between the two.

3.1.3. *Subduction of buoyancy features*

We then further incorporate (model V) the three pieces of overthickened oceanic crusts associated with the Inca Plateau, Nazca Ridge, and Juan Fernandez Ridge (Fig. 1) whose subduction started since late Miocene (Gutscher et al., 1999a; Ramos and Folguera, 2009) (Fig. 2a). The extra positive buoyancy from these features relative to the ambient mantle causes additional flattening of the slabs in Peru and Central Chile, greatly improving the fit to the *Slab1.0* contours (Fig. 3d, e). The predictions for the Central Chile and Southern Peru flat slabs are almost exact, given the observation that it is the hydrodynamic suction from the continent that slightly over-predicts the slab dip at 100 km depth between 20°S and 30°S (Fig. 3c, d). The amount of flattening in Northern Peru at 250 km depth is still slightly under predicted (Fig. 3e), and this is likely related to the under-estimation of suction force due to the uncertain geometry of Amazonia Craton. Overall, compared with model IV where only seafloor age variation and dynamic suction are considered (Fig. 3d), the buoyancy features contribute to slab

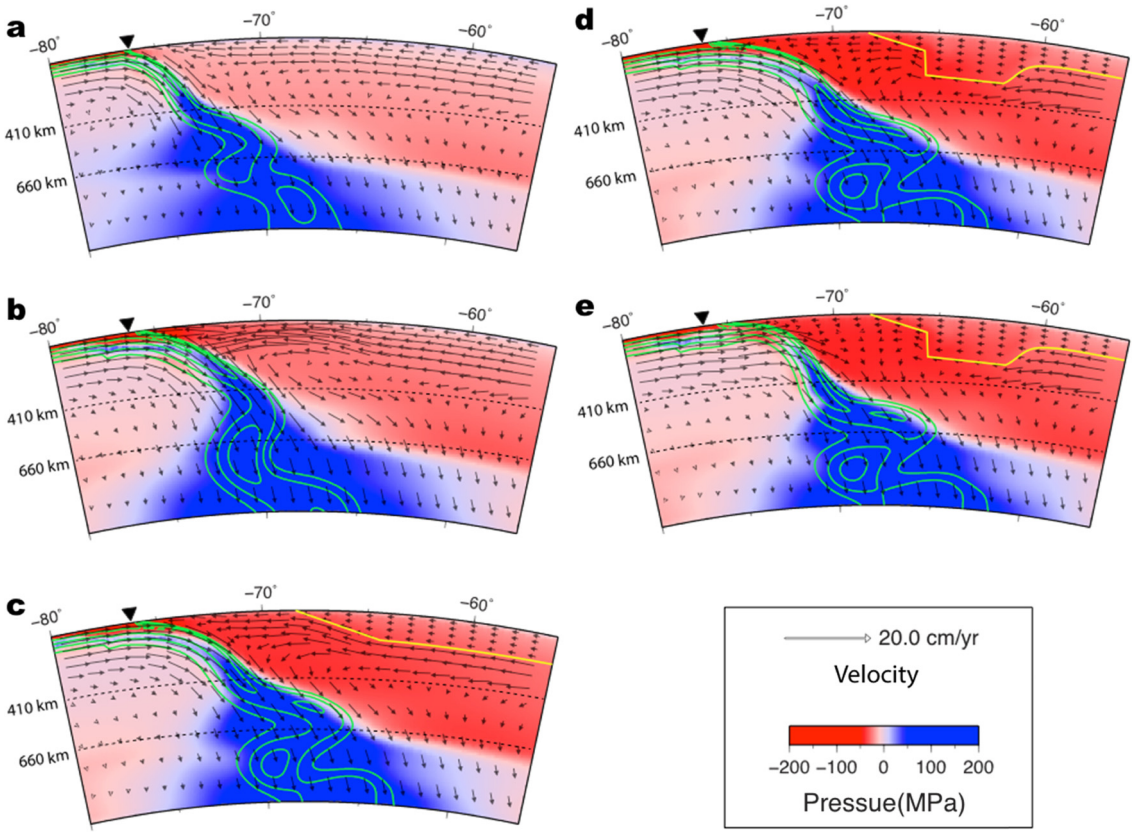

Fig. 8. Cross sections showing the dynamic pressure distribution at 15°S for model (a) I, (b) II, (c) III, (d) IV and (e) V. Arrows represent mantle velocities. Yellow thick lines outline the overriding plate. Solid green contours indicate slab isotherms with an increment of 100 °C. The dynamic pressure within the mantle wedge is progressively lowered from model I to model IV, indicating an increasing hydrodynamic suction. Notice that the mantle flow above the slab is mainly concentrated in the asthenosphere when a high-viscosity overriding plate is present. (For interpretation of the references to color in this figure legend, the reader is referred to the web version of this article.)

flattening at much smaller spatial scales (<500 km), comparable to the widths of these buoyancy features (Fig. 5a). We emphasize that the magnitudes of the background mantle viscosity and slab strength affect the overall slab dip along the entire trench but contribute little to the local variations of slab dip angle. So we utilize the same viscosity structure for all five models.

Besides the spatial scales, the temporal effect of subducting buoyancy features also differs from that of continental suction. Since the suction force resulting from the overriding plate exists throughout the subduction history, it exerts a prolonged influence on the subducting slab, which is reflected as a continuous reduction of slab dip angle over depth (thus time) in models III and IV relative to that in model II (Figs. 3, 8). The addition of aseismic ridges, however, affects the slab dip angle only since their initial subduction during the late Miocene, which corresponds to ~500 km depth at the present. That also explains why there is almost no difference between model IV and model V in slab geometry at greater depths (Figs. 3, 6, 8).

One of the most significant structural differences between our results and earlier studies is the development of a tear inside the flat slab associated with the subduction of buoyancy features (Fig. 9). Due to the progressive accumulation of strain at the down-dip side and the two flanks of the aseismic ridge during subduction, the flat slab is highly deformed internally and eventually a slab hole forms. The two pairs of spines in the outline of slab dip angle distribution at ~13°S and ~31°S in Fig. 5a are caused by these slab holes (Figs. 3e, 5b and 9). In order to be comparable to the Slab 1.0 contours that are spatially interpolated from the seismicity distribution, we also interpolated these parts of the slab dip angle using dashed lines (Fig. 5a). This way, we could see more clearly the small spatial scales (<500 km) of slab flattening due to the extra buoyancy of these over-thickened oceanic crusts (Fig. 5a, b).

Analysis of the temporal evolution of flat slabs in model V suggests that the formation of flat slabs was usually delayed by several million years relative to the start of buoyancy-feature subduction. This reflects the 3D structure of a flat slab that consumes the earlier subducted portion of the buoyancy feature to 'raise' the slab relative to its surroundings, consistent with the results of analog models (Espurt et al., 2008). For example, the Nazca Ridge entered the trench at ~12 Ma, but the slab reached its flattest state at ~4 Ma (Fig. 9), which is also consistent with the cessation of arc volcanism at this time (Fig. 9). A similar situation is seen during the subduction of the Inca Plateau (Fig. 9).

3.2. The predicted present-day flat slabs

Fig. 10 shows six different vertical cross sections of our best-fit model (i.e. model V). We compare this model prediction with upper mantle Benioff zone geometry using *slab 1.0* (Hayes et al., 2012) and seismicity catalog from IRIS (http://service.iris.edu/fdsnws/event/docs/1/builder/). Three cross sections through the flat-slab segments (Fig. 10a, b, f) and three through the normal subduction parts (Fig. 10c–e) are shown. As can be seen, the predicted slab geometry fits the Benioff zone generally well both in the normal and flat slab segments (Fig. 3e, 10). We do not fine-tune the slab strength and overriding plate thickness, in order to better match these profiles, since we mainly focus on the first order effect of the different physical mechanisms for slab flattening, and these models (I–V) demonstrate a clear improve-

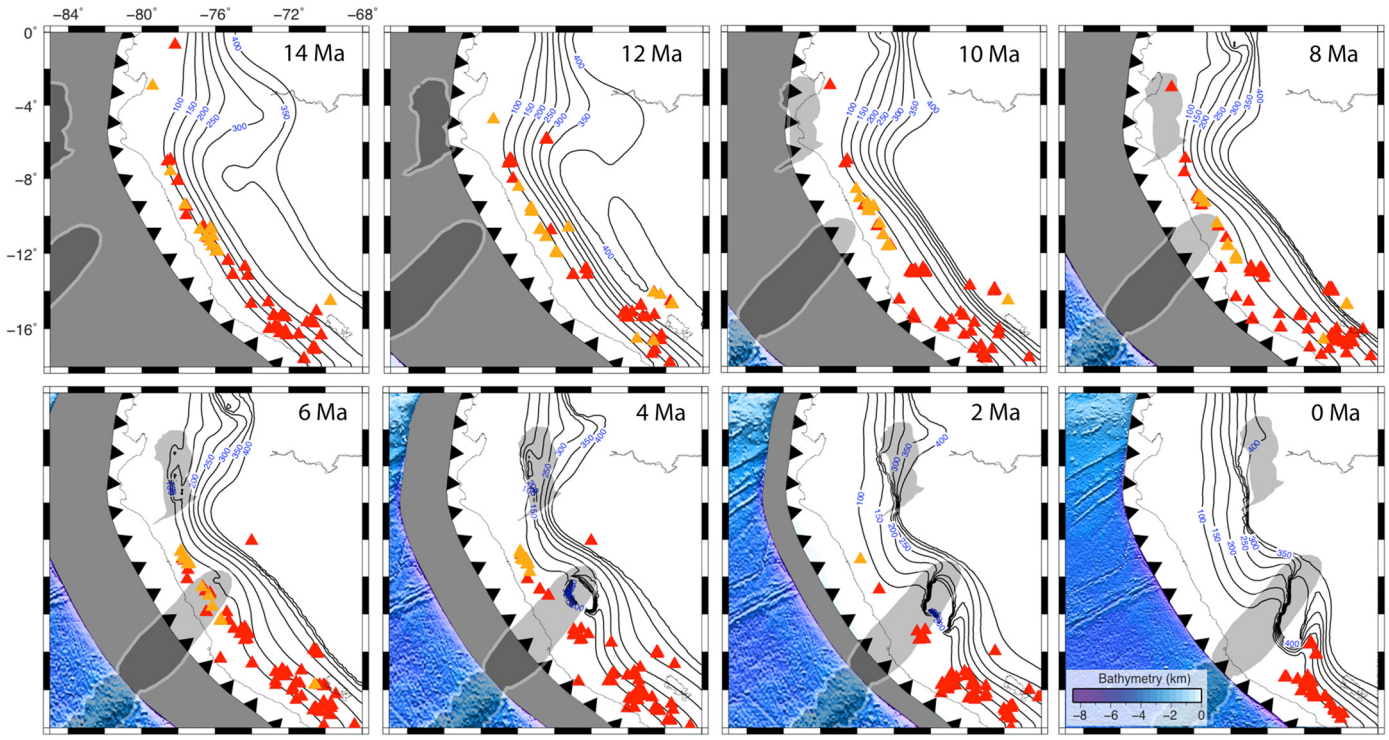

Fig. 9. The evolution of slab geometry beneath Peru from 14 Ma to present day. Black lines represent the slab upper surface (300 °C cooler than the ambient mantle) at different depths. Dark gray patterns show the reconstructed locations of the Inca Plateau and the Nazca Ridge. Light gray area represents now-subducted seafloors. Red triangles indicate the location of extrusive volcanism, while orange triangles represent that of intrusive volcanism. A slab hole forms since 6 Ma during the Nazca Ridge subduction. Note the delay between initial buoyancy feature subduction and flat slab formation. (For interpretation of the references to color in this figure legend, the reader is referred to the web version of this article.)

ment toward the final prediction of the observed slab geometry.

In central Chile (Fig. 10f), the Juan Fernandez Ridge has effectively flattened the slab locally. This predicted slab geometry fits both the *slab 1.0* contour and the seismicity pattern above 150 km depth very well, but not below this depth (Fig. 10f). We suggest that this misfit is due to the interpolated nature of *slab 1.0* below 150 km depth, where there is no seismicity between 250 and 500 km along the entire South American trench (Hayes et al., 2012). The same situation and reasoning apply to the Peruvian flat slab, where the Benioff zone is interpolated with depth (Fig. 10a, b). However, a confirmed mismatch in the predicted Peruvian flat slab is that its overall depth is slightly larger compared to the Benioff zone at <200 km depth. This is likely due to two reasons: 1) The buoyancy of Inca Plateau and Nazca Ridge is insufficient to cause a wide flat slab as observed; 2) A larger continental suction is needed in order to generate a shallower slab.

Significantly, our study reveals some important differences from earlier 2-D simulations on flat-slab formation. According to the traditional view, subduction of a buoyancy feature (e.g., van Hunen et al., 2002) or suction from a thick craton (Manea et al., 2012) would result in a local decrease of dip angle inside a continuous slab. Our results, however, suggest that the down-dip part of the flat-slab steepens abruptly with increasing depth (Fig. 10a, b and f). This increase of slab dip below the flat slab is also consistent with analog model for buoyancy feature subduction (Martinod et al., 2005) and confirmed by tomographic images (Gutscher et al., 2000). This geometry variation reflects the reduced sinking speed of the flattening slab segment relative to surrounding slabs, and this different motion ultimately results in the slab holes as discussed earlier (e.g., Fig. 9). These apparent 3D effects are missing in earlier 2D models due to the assumption of infinite length in the third dimension.

4. Discussion and conclusions

According to our study, the modern flat slab segments in South America are caused by a combination of seafloor age variation, hydrodynamic suction from the overriding plate, and subduction of buoyancy features. This may explain why there is a lack of clear correlation between seafloor age and slab dip global-wide (Jarrard, 1986; Lallemand et al., 2005; Cruciani et al., 2005). We find that with seafloor age >30 Ma, older seafloor age (<60 Ma in South America) tends to cause flatter subduction (model I vs. model S), which is consistent with earlier modeling work (Billen and Hirth, 2007). This suggests that slab strength dominates negative buoyancy in controlling slab dip in this age range. However, with seafloor age <30 Ma, we find that younger seafloor age leads to shallower slab dip (model I vs. model II), which likely results from the overall small negative buoyancy of the young slabs and the stronger effect of the buoyant oceanic crust, relative to older slabs. This conclusion on how seafloor age influences slab dip, however, should be subject to future verification.

The flexibility of data assimilation models also allows us to quantify the respective roles of the overriding plate and subducting buoyancy features on influencing the slab dip angle. According to our results, hydrodynamic suction only controls the long-wavelength variation of slab dip angle along trench (Figs. 3, 5). In particular, a uniformly thick overriding plate causes a systematic reduction of the slab dip angle (Fig. 5); the incorporation of cratons induces additional perturbations to the slab dip over ~1000 km spatial scale, which is considerably larger than that induced by the subduction of buoyancy features (Fig. 5). As a result, the sharp kinks of the slab contour at 100 km depth in Chile and Peru (Fig. 1)

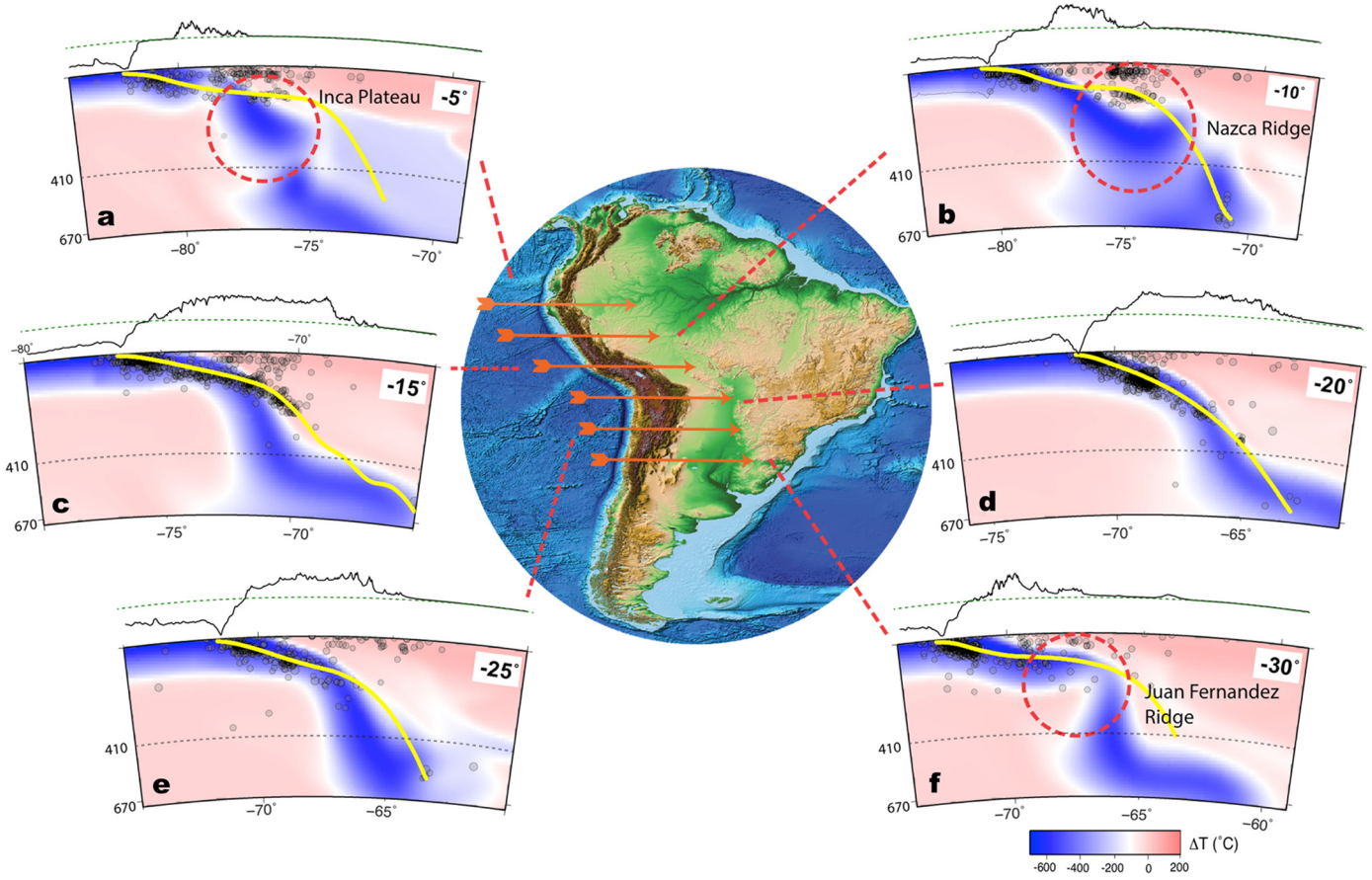

Fig. 10. Cross sections of the best-fit model from 5° to 30°S at an interval of 5°. Orange arrows mark the location of these cross sections. In each cross section, background color represents the temperature field with the yellow lines indicating the interpolated Benioff zone from *slab 1.0* (Hayes et al., 2012). Gray circles represent the locations of earthquakes with magnitude >4.0 from IRIS earthquake catalog for years from 1970 to 2015. Black lines above each cross section delineate the topography, with the vertical scale amplified by 20 times. Note the overall match of the slab geometry to both individual seismicity and *slab 1.0 contour*. (For interpretation of the references to color in this figure legend, the reader is referred to the web version of this article.)

are most likely caused by the subduction of two narrow aseismic ridges, since the suction from nearby cratons would have elevated a much wider segment of the slab.

It is worth noting that, in our model, flattening of the Peruvian slab is slightly under-predicted (Fig. 3e). This requires either further reduced slab density or a stronger interpolate coupling across this region. The latter case could result from either a thicker overriding plate or a higher mantle-wedge viscosity (Manea and Gurnis, 2007; Rodríguez-González et al., 2012, 2014) than those assumed in our models. In reality, the subduction of buoyancy features could have flattened the slab to a critical angle, which then initiated a positive feedback between slab flattening and increased suction (Stevenson and Turner, 1977; Taramón et al., 2015), further reducing the slab dip angle (Fig. 1). As shown in a recent modeling study with non-linear rheology (Taramón et al., 2015), this positive feedback could have formed a permanent flat slab in Peru where the seafloor is relatively young (Fig. 2).

There is still an ongoing debate on whether subducting buoyancy features can cause flat slabs. While earlier 2D numerical models (e.g., van Hunen et al., 2000) support this hypothesis, a recent study (Gerya et al., 2009) suggests that aseismic ridges with moderate sizes could not generate flat slabs. Our 3D models with data assimilation demonstrate that the subduction of buoyancy features clearly contributes to the formation of the localized flat slabs in Peru and Chile (Fig. 5a). By simultaneously considering other physical mechanisms, we show that although down-going buoyancy features can effectively reduce the slab dip angle, the presence of other mechanisms such as dynamic suction is also necessary in order to predict the exact amount of flattening. The inadequate flattening of the Peruvian slab in our model represents a potential example for the need of additional lifting forces besides slab buoyancy.

The same reasoning may help to explain the poor spatial and temporal correlation between subducting buoyancy features and observed flat slabs (Skinner and Clayton, 2013), since buoyancy perturbation within the down-going slab is not the only driving force for flat slabs to form. Another possible reason is related to the temporal delay between flab slab formation and the initiation of buoyancy feature subduction. For example, the Juan Fernandez Ridge started to subduct at ~12 Ma (Yáñez et al., 2002), but the cessation of volcanism began at ~5 Ma (Espurt et al., 2008). A similar delay is also observed in Peru as discussed earlier (Fig. 9). This may further explain why the subduction of Carnegie Ridge and Iquique Ridge do not correlate with on-going flat slabs, given the short history of the Iquique Ridge subduction (<2 Ma, Rosenbaum et al., 2005) and the nascent slab flattening process associated with the Carnegie Ridge (Gutscher et al., 1999b). In addition, the poor correlation between flat slabs and buoyancy feature subduction can also be due to the tendency of the slab to stay flat long after the subduction of the buoyancy feature, as observed in both analog (Martinod et al., 2005) and numerical (Taramón et al., 2015) models. In this case, an extant flat slab could be due to an ancient buoyancy feature subduction.

The volcanic history in Peru provides useful constraints on the development of flat slabs during the subduction of buoyancy features. Prior to 4 Ma, the arc volcanism is largely continuous

in Southern Peru. After this time, a clearly defined volcanic gap emerged (Fig. 9), which coincides with the slab flattening due to the Nazca Ridge subduction. While this confirms the general belief on the relation between volcanic gap and flat slab (Nur and Ben-Avraham, 1981; McGeary et al., 1985; Ramos and Folguera, 2009), our model further shows a significant delay of slab flattening and the cessation of volcanism, relative to the initial subduction of the buoyancy feature. Furthermore, a possible delay by ~2–4 Myr of the volcanic gap formation from initial slab flattening is also observed (Fig. 9). If correct, this may reflect the secular cooling of the mantle wedge above a flat slab (van Hunen et al., 2002).

On the other hand, there seems to be long-lived magmatic quiescence between the equator and 6°S (Fig. 9). Subduction of the Inca Plateau further cleared out some sporadic volcanisms along these latitudes that were erupted prior to 8 Ma (Fig. 9). Temporally and spatially, this lack of volcanism correlates with an overall shallow to flat slab segment that has been in existence for more than 14 Myr (Fig. 9). This abnormal slab segment is not due to the subduction of buoyancy features. Possible reasons for its formation may include the small trench curvature, past plate motions, and the earlier subduction history, given the presence of this slab feature in most models presented (Fig. 3). Since all our models use the same plate kinematics, we could not separately evaluate the dependence of slab dip on the overriding plate motion (Jarrard, 1986; van Hunen et al., 2000; Lallemand et al., 2005), or trench curvature (Tovish and Gerald, 1978; Schellart et al., 2007). A better understanding on this phenomenon will require future modeling efforts.

Finally, we emphasize that future research is necessary to further verify the dynamics of flat slab subduction. An important aspect is mantle rheology. In our models, we search for an effective viscosity structure that best matches the present-day mantle seismic image. A more physically self-consistent mantle rheology is non-linear viscosity including pseudo-plasticity (Bello et al., 2015) and strain rate-weakening (Taramón et al., 2015). However, to what extent the non-linear rheology can approximate subduction dynamics is still debated (Stegman et al., 2006; Stadler et al., 2010; Liu and Stegman, 2011; Arrial and Billen, 2013), which is likely due to the incapability of any single rheology to capture the natural complexity of the Earth. Since we are modeling the long-term subduction history of South America by assimilating many different data types, it is impractical to include such a complex rheology into our model. Future research, therefore, should focus on improved data assimilation techniques and more efficient computation methods.

Acknowledgement

We thank Xiaodong Song, Jay Bass, Craig Lundstrom and William Guenthner for helpful discussions. The numerical models are performed using CitcomS (www.geodynamics.org) and GPlates (www.gplates.org). Figures are prepared using the GMT software package (https://www.soest.hawaii.edu/gmt/). This work is supported by NSF grant EAR-1345135.

References

Anderson, M., Alvarado, P., Zandt, G., Beck, S., 2007. Geometry and brittle deformation of the subducting Nazca Plate, Central Chile and Argentina. Geophys. J. Int. 171 (1), 419–434.

Arriagada, C., Roperch, P., Mpodozis, C., Cobbold, P.R., 2008. Paleogene building of the Bolivian Orocline: tectonic restoration of the central Andes in 2-D map view. Tectonics 27 (6).

Arrial, P.A., Billen, M.I., 2013. Influence of geometry and eclogitization on oceanic plateau subduction. Earth Planet. Sci. Lett. 363, 34–43.

Barazangi, M., Isacks, B.L., 1976. Spatial distribution of earthquakes and subduction of the Nazca plate beneath South America. Geology 4 (11), 686–692.

Barazangi, M., Isacks, B.L., 1979. Subduction of the Nazca plate beneath Peru: evidence from spatial distribution of earthquakes. Geophys. J. Int. 57 (3), 537–555.

Bello, L., Coltice, N., Tackley, P.J., Müller, R.D., Cannon, J., 2015. Assessing the role of slab rheology in coupled plate–mantle convection models. Earth Planet. Sci. Lett. 430, 191–201.

Billen, M.I., Hirth, G., 2007. Rheologic controls on slab dynamics. Geochem. Geophys. Geosyst. 8 (8).

Boyden, J.A., Müller, R.D., Gurnis, M., Torsvik, T.H., Clark, J.A., Turner, M., Ivey-Law, H., Watson, R.J., Cannon, J.S., 2011. Next-generation plate-tectonic reconstructions using GPlates. In: Geoinformatics: Cyberinfrastructure for the Solid Earth Sciences, pp. 95–114.

Cloos, M., 1993. Lithospheric buoyancy and collisional orogenesis: subduction of oceanic plateaus, continental margins, island arcs, spreading ridges, and seamounts. Geol. Soc. Am. Bull. 105 (6), 715–737.

Cruciani, C., Carminati, E., Doglioni, C., 2005. Slab dip vs. lithosphere age: no direct function. Earth Planet. Sci. Lett. 238 (3), 298–310.

Davies, D.R., Davies, J.H., Hassan, O., Morgan, K., Nithiarasu, P., 2007. Investigations into the applicability of adaptive finite element methods to two-dimensional infinite Prandtl number thermal and thermochemical convection. Geochem. Geophys. Geosyst. 8 (5).

Espurt, N., Funiciello, F., Martinod, J., Guillaume, B., Regard, V., Faccenna, C., Brusset, S., 2008. Flat subduction dynamics and deformation of the South American plate: insights from analog modeling. Tectonics 27 (3).

Flament, N., Gurnis, M., Williams, S., Seton, M., Skogseid, J., Heine, C., Müller, R.D., 2014. Topographic asymmetry of the South Atlantic from global models of mantle flow and lithospheric stretching. Earth Planet. Sci. Lett. 387, 107–119.

Fukao, Y., Obayashi, M., 2013. Subducted slabs stagnant above, penetrating through, and trapped below the 660 km discontinuity. J. Geophys. Res., Solid Earth 118 (11), 5920–5938.

Gerya, T.V., Fossati, D., Cantieni, C., Seward, D., 2009. Dynamic effects of aseismic ridge subduction: numerical modelling. Eur. J. Mineral. 21 (3), 649–661.

Gurnis, M., Turner, M., Zahirovic, S., DiCaprio, L., Spasojevic, S., Müller, R.D., Boyden, J., Seton, M., Manea, V.C., Bower, D.J., 2012. Plate tectonic reconstructions with continuously closing plates. Comput. Geosci. 38 (1), 35–42.

Gurnis, M., Turner, M., Bower, D., Flament, N.E., Müller, R.D., 2013. Advancing cyberinfrastructure for plate reconstructions: present day mantle structure and the stratigraphic architecture of continents as signals of a dynamic Earth. Abstr. Program – Geol. Soc. Am. 45 (7), 233.

Gutscher, M.A., Olivet, J.L., Aslanian, D., Eissen, J.P., Maury, R., 1999a. The "lost Inca Plateau": cause of flat subduction beneath Peru? Earth Planet. Sci. Lett. 171 (3), 335–341.

Gutscher, M.A., Malavieille, J., Lallemand, S., Collot, J.Y., 1999b. Tectonic segmentation of the North Andean margin: impact of the Carnegie Ridge collision. Earth Planet. Sci. Lett. 168 (3), 255–270.

Gutscher, M.A., Spakman, W., Bijwaard, H., Engdahl, E.R., 2000. Geodynamics of flat subduction: seismicity and tomographic constraints from the Andean margin. Tectonics 19 (5), 814–833.

Hayes, G.P., Wald, D.J., Johnson, R.L., 2012. Slab1.0: a three-dimensional model of global subduction zone geometries. J. Geophys. Res., Solid Earth (1978–2012) 117 (B1).

Huene, R.V., Corvalán, J., Flueh, E.R., Hinz, K., Korstgard, J., Ranero, C.R., Weinrebe, W., 1997. Tectonic control of the subducting Juan Fernández Ridge on the Andean margin near Valparaiso, Chile. Tectonics 16 (3), 474–488.

Isacks, B.L., 1988. Uplift of the central Andean plateau and bending of the Bolivian orocline. J. Geophys. Res., Solid Earth (1978–2012) 93 (B4), 3211–3231.

Jarrard, R.D., 1986. Relations among subduction parameters. Rev. Geophys. 24 (2), 217–284.

Jones, C.H., Farmer, G.L., Sageman, B., Zhong, S., 2011. Hydrodynamic mechanism for the Laramide orogeny. Geosphere 7 (1), 183–201.

Kay, S.M., Mpodozis, C., 2002. Magmatism as a probe to the Neogene shallowing of the Nazca plate beneath the modern Chilean flat-slab. J. South Am. Earth Sci. 15 (1), 39–57.

Kley, J., Monaldi, C.R., 1998. Tectonic shortening and crustal thickness in the Central Andes: how good is the correlation? Geology 26 (8), 723–726.

Klotz, J., Khazaradze, G., Angermann, D., Reigber, C., Perdomo, R., Cifuentes, O., 2001. Earthquake cycle dominates contemporary crustal deformation in Central and Southern Andes. Earth Planet. Sci. Lett. 193 (3), 437–446.

Lallemand, S., Heuret, A., Boutelier, D., 2005. On the relationships between slab dip, back-arc stress, upper plate absolute motion, and crustal nature in subduction zones. Geochem. Geophys. Geosyst. 6 (9).

Liu, L., Stegman, D.R., 2011. Segmentation of the Farallon slab. Earth Planet. Sci. Lett. 311 (1), 1–10.

Loewy, S.L., Connelly, J.N., Dalziel, I.W., 2004. An orphaned basement block: the Arequipa-Antofalla Basement of the central Andean margin of South America. Geol. Soc. Am. Bull. 116 (1–2), 171–187.

Manea, V., Gurnis, M., 2007. Subduction zone evolution and low viscosity wedges and channels. Earth Planet. Sci. Lett. 264 (1), 22–45.

Manea, V.C., Pérez-Gussinyé, M., Manea, M., 2012. Chilean flat slab subduction controlled by overriding plate thickness and trench rollback. Geology 40 (1), 35–38.

Marquardt, H., Miyagi, L., 2015. Slab stagnation in the shallow lower mantle linked to an increase in mantle viscosity. Nat. Geosci. 8 (4), 311–314.
Martinod, J., Funiciello, F., Faccenna, C., Labanieh, S., Regard, V., 2005. Dynamical effects of subducting ridges: insights from 3-D laboratory models. Geophys. J. Int. 163 (3), 1137–1150.
Mason, W.G., Moresi, L., Betts, P.G., Miller, M.S., 2010. Three-dimensional numerical models of the influence of a buoyant oceanic plateau on subduction zones. Tectonophysics 483 (1), 71–79.
McGeary, S., Nur, A., Ben-Avraham, Z., 1985. Spatial gaps in arc volcanism: the effect of collision or subduction of oceanic plateaus. Tectonophysics 119 (1), 195–221.
McQuarrie, N., 2002. Initial plate geometry, shortening variations, and evolution of the Bolivian orocline. Geology 30 (10), 867–870.
Müller, R.D., Sdrolias, M., Gaina, C., Roest, W.R., 2008. Age, spreading rates, and spreading asymmetry of the world's ocean crust. Geochem. Geophys. Geosyst. 9 (4).
Nur, A., Ben-Avraham, Z., 1981. Volcanic gaps and the consumption of aseismic ridges in South America. Geol. Soc. Am. Mem. 154, 729–740.
O'Driscoll, L.J., Humphreys, E.D., Saucier, F., 2009. Subduction adjacent to deep continental roots: enhanced negative pressure in the mantle wedge, mountain building and continental motion. Earth Planet. Sci. Lett. 280 (1), 61–70.
O'Driscoll, L.J., Richards, M.A., Humphreys, E.D., 2012. Nazca–South America interactions and the late Eocene–late Oligocene flat-slab episode in the central Andes. Tectonics 31 (2).
Oncken, O., Hindle, D., Kley, J., Elger, K., Victor, P., Schemmann, K., 2006. Deformation of the central Andean upper plate system—facts, fiction, and constraints for plateau models. In: The Andes. Springer, Berlin, Heidelberg, pp. 3–27.
Pennington, W.D., 1981. Subduction of the eastern Panama Basin and seismotectonics of northwestern South America. J. Geophys. Res., Solid Earth (1978–2012) 86 (B11), 10753–10770.
Ramos, V.A., Cristallini, E.O., Pérez, D.J., 2002. The Pampean flat-slab of the Central Andes. J. South Am. Earth Sci. 15 (1), 59–78.
Ramos, V.A., Folguera, A., 2009. Andean flat-slab subduction through time. Geol. Soc. (Lond.) Spec. Publ. 327 (1), 31–54.
Roda, M., Marotta, A.M., Spalla, M.I., 2011. The effects of the overriding plate thermal state on the slab dip in an ocean–continent subduction system. C. R. Géosci. 343 (5), 323–330.
Rodríguez-González, J., Negredo, A.M., Billen, M.I., 2012. The role of the overriding plate thermal state on slab dip variability and on the occurrence of flat subduction. Geochem. Geophys. Geosyst. 13 (1).
Rodríguez-González, J., Billen, M.I., Negredo, A.M., 2014. Non-steady-state subduction and trench-parallel flow induced by overriding plate structure. Earth Planet. Sci. Lett. 401, 227–235.
Rosenbaum, G., Giles, D., Saxon, M., Betts, P.G., Weinberg, R.F., Duboz, C., 2005. Subduction of the Nazca Ridge and the Inca Plateau: insights into the formation of ore deposits in Peru. Earth Planet. Sci. Lett. 239 (1), 18–32.
Schellart, W.P., Freeman, J., Stegman, D.R., Moresi, L., May, D., 2007. Evolution and diversity of subduction zones controlled by slab width. Nature 446 (7133), 308–311.
Seton, M., Müller, R.D., Zahirovic, S., Gaina, C., Torsvik, T., Shephard, G., Talsma, A., Gurnis, M., Turnes, M., Maus, S., Chandler, M., 2012. Global continental and ocean basin reconstructions since 200 Ma. Earth-Sci. Rev. 113 (3), 212–270.
Skinner, S.M., Clayton, R.W., 2013. The lack of correlation between flat slabs and bathymetric impactors in South America. Earth Planet. Sci. Lett. 371, 1–5.
Stadler, G., Gurnis, M., Burstedde, C., Wilcox, L.C., Alisic, L., Ghattas, O., 2010. The dynamics of plate tectonics and mantle flow: from local to global scales. Science 329 (5995), 1033–1038.
Stegman, D.R., Freeman, J., Schellart, W.P., Moresi, L., May, D., 2006. Influence of trench width on subduction hinge retreat rates in 3-D models of slab rollback. Geochem. Geophys. Geosyst. 7 (3).
Stevenson, D.J., Turner, J.S., 1977. Angle of subduction. Nature 270, 334–336.
Tackley, P.J., King, S.D., 2003. Testing the tracer ratio method for modeling active compositional fields in mantle convection simulations. Geochem. Geophys. Geosyst. 4 (4).
Tan, E., Choi, E., Thoutireddy, P., Gurnis, M., Aivazis, M., 2006. GeoFramework: coupling multiple models of mantle convection within a computational framework. Geochem. Geophys. Geosyst. 7 (6).
Taramón, J.M., Rodríguez-González, J., Negredo, A.M., Billen, M.I., 2015. Influence of cratonic lithosphere on the formation and evolution of flat slabs: insights from 3-D time-dependent modeling. Geochem. Geophys. Geosyst. 16 (9), 2933–2948.
Tovish, A., Gerald, S., 1978. Island arc curvature, velocity of convergence and angle of subduction. Geophys. Res. Lett. 5 (5), 329–332.
van Hunen, J., van den Berg, A.P., Vlaar, N.J., 2000. A thermo-mechanical model of horizontal subduction below an overriding plate. Earth Planet. Sci. Lett. 182 (2), 157–169.
van Hunen, J., Van Den BERG, A.P., Vlaar, N.J., 2002. On the role of subducting oceanic plateaus in the development of shallow flat subduction. Tectonophysics 352 (3), 317–333.
Yáñez, G., Cembrano, J., Pardo, M., Ranero, C., Selles, D., 2002. The Challenger–Juan Fernández–Maipo major tectonic transition of the Nazca–Andean subduction system at 33–34°S: geodynamic evidence and implications. J. South Am. Earth Sci. 15 (1), 23–38.
Zhong, S., Zuber, M.T., Moresi, L., Gurnis, M., 2000. Role of temperature-dependent viscosity and surface plates in spherical shell models of mantle convection. J. Geophys. Res., Solid Earth (1978–2012) 105 (B5), 11063–11082.